PHYSICAL REVIEW MATERIALS **7**, 113608 (2023)

Crystal plasticity finite element simulation of lattice rotation and x-ray diffraction during laser shock compression of tantalum

P. Avraam,[1] D. McGonegle,[1,*] P. G. Heighway,[2] C. E. Wehrenberg,[3] E. Floyd,[1] A. J. Comley,[1]
J. M. Foster,[1] S. D. Rothman,[1] J. Turner,[1] S. Case,[1] and J. S. Wark[2]
[1]*AWE, Aldermaston, Reading RG7 4PR, United Kingdom*
[2]*Department of Physics, Clarendon Laboratory, University of Oxford, Parks Road, Oxford OX1 3PU, United Kingdom*
[3]*Lawrence Livermore National Laboratory, Livermore, California 94550, USA*

(Received 16 August 2021; accepted 6 June 2023; published 27 November 2023)

We present a crystal plasticity model tailored for high-pressure, high-strain-rate conditions that uses a multiscale treatment of dislocation-based slip kinetics. We use this model to analyze the pronounced plasticity-induced lattice rotations observed in shock-compressed polycrystalline tantalum via *in situ* x-ray diffraction. By making direct comparisons between experimentally measured and simulated texture evolution, we can explain how the details of the underlying slip kinetics control the degree of lattice rotation that ensues. Specifically, we show that only the highly nonlinear kinetics caused by dislocation *nucleation* can explain the magnitude of the rotation observed under shock compression. We demonstrate a good fit between our crystal plasticity model and x-ray diffraction data and exploit the data to quantify the dislocation nucleation rates that are otherwise poorly constrained by experiment in the dynamic compression regime.

DOI: 10.1103/PhysRevMaterials.7.113608

I. INTRODUCTION

When a crystal is uniaxially shock compressed beyond the elastic limit, plastic deformation mechanisms are activated. The high rates of plastic strain observed at the shock front cannot be mediated by the motion of preexisting dislocations—dislocation density must grow rapidly during deformation at the shock front or other plastic deformation mechanisms, such as deformation twinning, must occur. This deformation activity is anisotropic, occurring predominantly in specific characteristic crystallographic planes and directions within the single-crystal grains that make up the polycrystal, resulting in lattice rotation (texture evolution).

An understanding of plastic deformation mechanisms and their kinetics spanning the relevant length scales has long been sought. Insight into the underlying physics of the resistance of materials to plastic flow at ultrahigh strain rates and pressures is of direct relevance to a range of phenomena, including planetary impact scenarios [1–3] and inertial confinement fusion [4]. In the latter case, the means by which material strength reduces the growth rate of hydrodynamic instabilities in a solid is of particular interest. Integrated experiments that interrogate the growth of the Rayleigh-Taylor (RT) instability at strain rates of order 10^6–10^7 s^{-1} [5,6] show good agreement with certain continuum-based approaches such as the Livermore multiscale strength (LMS) model [6,7].

While such integrated RT experiments give some information on overall strength under these extreme conditions, lattice-level insights into specific plasticity mechanisms cannot be directly ascertained. By contrast, discernment of plasticity-related activity at this atomistic scale *can* be obtained in experiments that utilize ultrafast *in situ* x-ray diffraction (XRD) to study laser-driven material undergoing rapid plastic relaxation [8–10]. In particular, the seminal work of Wehrenberg *et al.* [11], using the Linac Coherent Light Source (LCLS) x-ray free-electron laser (XFEL) facility, exploited initially highly textured polycrystalline samples to measure large lattice rotations due to slip and deformation twinning during shock loading. The degree of rotation implied slip (or twinning) on mainly one system, but why this was the case in the experiment was not understood until this work. The authors compared their results with both a simple zero-dimensional single-slip analysis based on the "Schmid" kinematic framework [12]—with moderate success—and with the results of large-scale classical molecular dynamics (MD) simulations of single-crystal tantalum. However, it is now understood that the Schmid framework is fundamentally unsuited to describing lattice rotation under uniaxial compression [13] and, while MD simulations [13–18] have yielded significant insight over the past decade, they are limited in the length and timescales that they can reach due to their computational cost, which restricts their utility in addressing questions of texture evolution in polycrystals.

Moreover, the complex material states that result from rapid loading of crystals often leave complex diffractogram signatures that are difficult to interpret. Efforts have been made to reproduce diffraction signals from modeling: Debye-Scherrer diffraction has been reproduced from continuum models that make rather crude polycrystalline homogenization assumptions [19,20] and MD simulations have been used to isolate characteristic diffractogram signatures associated with different deformation modes [21–24]. Similar capability

---

[*] david.mcgonegle@awe.co.uk

©2023 American Physical Society

has been demonstrated using crystal plasticity finite element (CPFE) simulations of single crystals [25].

The CPFE method overcomes many of the limitations of mean-field methods and of MD. It provides a way to model polycrystals by explicitly accounting for the anisotropic plasticity and elasticity of individual grains, while being computationally efficient enough to account for realistically sized polycrystals with grain-grain interactions over representative timescales.

It is in the above context that we present results from CPFE simulations of the shock-compression experiment of Wehrenberg *et al.* on [110] fiber-textured tantalum. We use a dislocation-based model of slip kinetics [26] based closely on the LMS isotropic continuum strength model [7], which itself relies for its construction on input from dislocation dynamics (DD), MD, and quantum mechanical simulations, affording a bridge between atomistic and mesoscale simulations. By extending the LMS model to include a dislocation nucleation term, we find excellent, unprecedented agreement with the experimental data down to the lowest shock pressures explored in the experiment. Indeed, we find that the degree of lattice rotation cannot be explained without recourse to dislocation nucleation. We use the locus of rotation states as a function of shock pressure measured by Wehrenberg *et al.* to constrain dislocation nucleation rates in tantalum under extreme conditions. Wehrenberg *et al.*'s data are ideally suited to this task due to the complete absence of complicating nonplastic processes (e.g. phase transitions, recrystallization) in shock-compressed tantalum [11].

The paper is structured as follows. In Sec. II, we set out the structure of our crystal plasticity model, drawing particular attention to those of its features that differentiate it from existing models currently used to model tantalum under extreme loading conditions. We present the setup and results of our CPFE simulations in Secs. III and IV, respectively. We compare their predictions of the texture evolution of shocked tantalum polycrystals with diffraction-based measurements taken by Wehrenberg *et al.* and demonstrate strong agreement between the two up to shock pressures of 140 GPa. We provide a discussion of the results in Sec. V and conclude in Sec. VI.

II. CRYSTAL PLASTICITY MODEL

Our constitutive modeling approach comprises a dislocation-aware crystal plasticity model embedded within a finite-element-method framework. As is common for materials with isotropic and cubic symmetry [27], the model uses the assumption of fully decoupled hydrostatic and deviatoric responses. A nonlinear thermoelastic treatment is used for the hydrostatic part of the distortion via an equation-of-state model; the deviatoric distortion is modeled with single-crystal linear elasticity theory, with linear pressure and temperature dependence assumed for the independent elastic constants. Kinematics are based on the work of Bronkhorst *et al.* [28–31] and the dislocation-based slip-kinetics model we use is based closely on the viscoplastic isotropic multiscale model of Barton *et al.* [7]. To facilitate comparison with existing models, we now describe in detail the mathematical structure of our constitutive model.

A. Kinematics

Local deformation of the material is described by the the total deformation gradient $\mathbf{F}$, which is decomposed multiplicatively into its elastic and plastic components:

$$\mathbf{F} = \mathbf{F}_e\mathbf{F}_p, \tag{1}$$

where $\mathbf{F}_e$ and $\mathbf{F}_p$ are the elastic and plastic deformation gradient tensors, respectively. The elastic deformation gradient $\mathbf{F}_e$ describes the local deformation of the material's underlying crystal structure, which encodes both true distortion and lattice rotation. The lattice vector $\mathbf{a}_0$ is distorted according to the formula

$$\mathbf{a} = \mathbf{F}_e\mathbf{a}_0, \tag{2}$$

while lattice-plane normal vector $\hat{\mathbf{n}}_0$ distorts as

$$\hat{\mathbf{n}} = \frac{\hat{\mathbf{n}}_0\mathbf{F}_e^{-1}}{\left\|\hat{\mathbf{n}}_0\mathbf{F}_e^{-1}\right\|}. \tag{3}$$

To disentangle the effects of rotation and distortion, the deformation gradient may be decomposed using a polar decomposition of the form

$$\mathbf{F}_e = \mathbf{Q}_e\mathbf{U}_e, \tag{4}$$

where $\mathbf{U}_e$ is the symmetric *right elastic strain tensor* and $\mathbf{Q}_e$ is a rotation matrix. Lattice rotation was measured directly by Wehrenberg *et al.* using femtosecond x-ray diffraction, making $\mathbf{Q}_e$ the key point of comparison between our model and experiment. Details regarding exactly which of the components of $\mathbf{Q}_e$ were accessible in the relevant experimental geometry will be given in Sec. IV.

The evolution of the plastic deformation gradient $\mathbf{F}_p$ is expressed by the plastic velocity gradient $\mathbf{L}_p$, which takes the form [28–31]

$$\mathbf{L}_p = \dot{\mathbf{F}}_p\mathbf{F}_p^{-1} = \sum_{\alpha=1}^{12}\dot{\gamma}^{\alpha}\left(\mathbf{m}_0^{\alpha}\otimes\mathbf{n}_0^{\alpha}\right), \tag{5}$$

where $\dot{\gamma}^{\alpha}$ is the slip rate on slip system α, defined by its slip direction $\mathbf{m}_0^{\alpha}$ and its slip plane normal $\mathbf{n}_0^{\alpha}$.

When choosing which slip systems to include in our model, we considered evidence from a range of computational and experimental studies. In bcc crystals, slip has been empirically observed to occur in $\langle 111\rangle$ directions on a diverse set of slip planes including $\{112\}$, $\{110\}$, and $\{123\}$, as well as on non-low-index crystallographic planes (pencil glide), under low strain-rate loading [32]. However, prevailing evidence suggests that, in tantalum, slip is realized principally on the $\{112\}$ planes. Classical MD simulations [32,33] and quantum mechanical simulations [34] of screw dislocations in tantalum have suggested that, at absolute zero, its dislocations move in fundamental unit jumps along $\{112\}$ planes via composite motion along alternating $\{110\}$ planes. Large-scale MD simulations of deformation at finite temperature and high strain rate also suggest that slip on $\{112\}$ planes is dominant at high strain rates in tantalum [13,35,36]. This is further supported by slip-trace analysis of samples recovered from a single-crystal Taylor impact experiment and accompanying crystal plasticity modeling [37], which showed greater consistency with a model that assumed slip on $\{112\}$ planes only than with a model that assumed slip on a mixture of {112} and {110} planes. Finally, the x-ray diffraction results from Wehrenberg *et al.* that we discuss here are consistent with deformation (both slip and twinning) occurring predominantly on effective {112} planes. We know on the basis of slip kinematics that plastic flow on a {110} slip plane would necessarily result in a systematic broadening of the diffraction spot coming from the {110} planes orthogonal to the shock direction; no such effect was observed experimentally. Overall, the combination of computational and experimental evidence suggests that slip in tantalum takes place primarily on the {112} planes.

We should note that even a {112}-plane-dominated picture of plasticity is still somewhat ambiguous, because it is possible to obtain "effective" {112} slip by cooperative activity on two adjacent {110} planes in the $\langle 111\rangle$ zone. However, in the interest of parsimony, we have chosen to include in our model the smallest set of planes that can satisfactorily explain the data. For this reason, we choose to model only the 12 slip systems spanned by the slip directions $\{\mathbf{m}_0^\alpha\} = \langle 111\rangle$ and the set of $\{\mathbf{n}_0^\alpha\} = \langle 112\rangle$ slip planes containing these directions.

The rate at which slip takes place on each slip system, $\dot{\gamma}_\alpha$, is connected to the properties of the dislocations on that slip system via the kinematic equation of Orowan:

$$\dot{\gamma}^\alpha = \rho^\alpha b^\alpha v^\alpha. \tag{6}$$

Here, b^α is the magnitude of the Burgers vector, ρ^α is the mobile dislocation density, and v^α is the average velocity of mobile dislocations on slip system α. A polycrystal-averaged version of Orowan's equation is used in the LMS model; here, we retain the original, single-grain form so that individual crystallites may be modeled faithfully.

We will now discuss the constitutive laws that predict the evolution of the dislocation densities and velocities.

B. Kinetics

1. Dislocation mobility

Part of the strain-rate and temperature dependence of the viscoplastic model comes from the dislocation mobility law, which relates the effective resolved shear stress $\tau_{\mathrm{eff}}^\alpha$ acting on any given slip system to the resulting average velocity at which that system's dislocations move, $v^\alpha(\tau_{\mathrm{eff}}^\alpha)$. In this context, the "effective" shear stress is defined as the resolved shear stress (RSS) τ^α less an athermal isotropic work-hardening term:

$$\tau_{\mathrm{eff}}^\alpha = \langle |\tau^\alpha| - \lambda b C_{44}\sqrt{\rho_{\mathrm{tot}}}\rangle. \tag{7}$$

The first term in Eq. (7) is the usual bare RSS, calculated by projecting the Cauchy stress tensor σ onto the appropriate slip system via

$$\tau^\alpha = \sigma(\mathbf{m}^\alpha \otimes \mathbf{n}^\alpha), \tag{8}$$

where the stresses are calculated from the instantaneous elastic deformation state using elastic moduli of the form

$$C_{ij} = C_{0,ij} + m_{ij}T + \chi_{ij}P. \tag{9}$$

Here, the $C_{0,ij}$ are the elastic moduli at temperature $T = 0$ K and pressure $P = 0$ GPa and the m_{ij} and χ_{ij} are material constants parametrized against quantum mechanical simulations [38] and experimental data [39]. The second term in Eq. (7) is the evolving slip-system hardness due to forest obstacles, which is assumed to vary with the square root of the total dislocation density $\rho_{\mathrm{tot}} = \sum_\alpha \rho^\alpha$ according to the standard Taylor form. Implicit in Eq. (7) is the assumption of isotropic latent hardening, which implies that the activity on one slip system results in equal hardening of all potential slip systems. The braces $\langle\rangle$ in Eq. (7) indicate that $\langle x\rangle = x$ for $x > 0$, but $\langle x\rangle = 0$ for $x < 0$, such that $\tau_{\mathrm{eff}}^\alpha$ vanishes when τ^α does.

To build an expression for the dislocation velocity v^α as a function of $\tau_{\mathrm{eff}}^\alpha$, we fitted a mobility law to the results of MD simulations of mobile screw dislocations moving under applied shear stress (as was done by Barton *et al.* [7]) using the classical interatomic potential from Ref. [40]. The functional form that is used to represent the MD data on dislocation mobility is constructed as a harmonic average of two terms—a *thermal activation* term and a *phonon drag* term (denoted by subscripts T and D, respectively):

$$v^\alpha = \left[\left(v_{\mathrm{T}}^\alpha\right)^{-1} + \left(v_{\mathrm{D}}^\alpha\right)^{-1}\right]^{-1}. \tag{10}$$

The thermal activation term, which dominates at lower shear stresses, takes the Arrhenius-like form

$$v_{\mathrm{T}}^\alpha = \frac{v_0}{\exp\left[\frac{\Delta G_0}{k_B T}\left\langle 1 - \left\langle \frac{\tau_{\mathrm{eff}}^\alpha}{\tau_0\left(\frac{C_{44}}{C_{0,44}}\right)}\right\rangle^p\right\rangle^q\right] - 1}, \tag{11}$$

where v_0, τ_0 (Peierls stress), ΔG_0 (activation enthalpy), p and q (Peierls barrier shape parameters) are fitted material constants, and k_B is the Boltzmann constant. The drag term (relevant at large resolved shear stresses) takes the form

$$v_{\mathrm{D}}^\alpha = v_{\mathrm{off}} + (v_{\mathrm{s}} - v_{\mathrm{off}})\left(\frac{2}{\pi}\right)\arctan\left(\left\langle \frac{\pi}{2}\,\frac{\tau_{\mathrm{eff}}^\alpha - \tau_{\mathrm{off}}}{\tau_{0,\mathrm{D}}\left(\frac{C_{44}}{C_{0,44}}\right)}\right\rangle\right), \tag{12}$$

a purely phenomenological form that is nearly linear when $\tau_{\mathrm{eff}}^\alpha$ is small [7] and asymptotes towards the shear wave speed v_s at large $\tau_{\mathrm{eff}}^\alpha$, chosen for its ability to represent the underlying dislocation mobility data.

We finally note that screw dislocations in bcc materials exhibit the well-known twinning-antitwinning asymmetry on {112} planes, meaning dislocations are much more mobile when driven in one direction along that plane (the twinning direction) than in the opposite direction. To reflect this asymmetry in our model, we prevent dislocations from moving in the antitwinning sense, as was done in Ref. [31].

2. Dislocation density

The remaining strain rate and temperature dependence of crystal plasticity flows from the dynamics of the dislocation populations. In our model, dislocation density evolution is governed by the rate equation

$$\dot{\rho}^\alpha = \dot{\rho}_{\mathrm{mult}}^\alpha - \dot{\rho}_{\mathrm{ann}}^\alpha + \dot{\rho}_{\mathrm{nuc}}^\alpha, \tag{13}$$

where the three source terms model dislocation multiplication, annihilation, and nucleation, respectively. Our treatment of the former two processes is identical to that of the LMS model [7]:

$$\dot{\rho}_{\mathrm{mult}}^\alpha - \dot{\rho}_{\mathrm{ann}}^\alpha = R\left(1 - \frac{\rho^\alpha}{\rho_{\mathrm{sat}}^\alpha(\dot{\gamma}^\alpha)}\right)\dot{\gamma}^\alpha, \tag{14}$$

where R is a material parameter and $\rho_{\text{sat}}^{\alpha}$ is the strain-rate-dependent saturation value of the dislocation density on slip system α. The first term accounts for dislocation growth due to multiplication of preexisting dislocations (e.g., by the expansion of extant dislocation loops), which is assumed to be proportional to ρ^{α}. The second term accounts for dislocation-dislocation annihilation, which is assumed to scale quadratically with ρ^{α}. The saturation density $\rho_{\text{sat}}^{\alpha}$ in Eq. (14) was modeled using multiscale dislocation dynamics (DD) simulations in Ref. [7]. Following this work, we define a saturated mobile dislocation density for each slip system as

$$\rho_{\text{sat}}^{\alpha}(\dot{\gamma}^{\alpha}) = \rho_{\text{sat,min}} + \rho_{\text{sat,0}}\left(\frac{\dot{\gamma}^{\alpha}}{\dot{\gamma}_{\text{sat}}}\right)^{\frac{1}{N_{\text{sat}}}}, \tag{15}$$

with parameters fitted to their simulation data.

The third source term in Eq. (13) representing the nucleation of dislocations does not feature in the LMS model. However, we now have firm evidence from molecular dynamics simulations that under the ultrahigh strain rates pertinent to shock compression, nucleation—particularly *homogeneous* nucleation—forms an integral part of crystal plasticity. During the high-strain-rate conditions present in dynamic compression fronts, dislocations and twins can be nucleated either from existing crystal defects such as grain boundaries (heterogeneous nucleation) or—at extremely high strain rates—out of the crystal bulk (homogeneous nucleation). Heterogeneous nucleation dominates at lower shock pressures [16], while homogeneous nucleation becomes active only above a material-dependent threshold stress. Recent MD studies estimate that the threshold shock pressure for activation of homogeneous dislocation nucleation is ∼65 GPa [41] in tantalum loaded along [100]. Other studies predict the homogeneous nucleation of deformation twins occurs beyond shock pressures of 40 GPa for not only [110] loading [14], but other loading directions too [15,17]. The uniaxial shock compression path to ∼200 GPa realized by Wehrenberg *et al.* engenders shear stress states far beyond these predicted thresholds, meaning any attempt to model their experiment must at least countenance dislocation nucleation processes.

Motivated by the nucleation model of Austin *et al.* [42], we express the dislocation nucleation rate $\dot{\rho}_{\text{nuc}}^{\alpha}$ in the Arrhenius-like (and crystal-structure agnostic) form

$$\dot{\rho}_{\text{nuc}}^{\alpha} = \dot{\rho}_0 \exp\left\{-\frac{g_{\text{nuc}} C_{44} b^3}{k_B T}\left[1 - \frac{\tau_{\text{eff}}^{\alpha}}{\tau_{\text{nuc},0}\left(\frac{C_{44}}{C_{0,44}}\right)}\right]\right\}, \tag{16}$$

where $\tau_{\text{nuc},0}$ expresses the critical RSS for nucleation (at ambient pressure and temperature) and g_{nuc} is a material parameter. This treatment of dislocation nucleation in a mechanically metastable crystal is analogous to classical nucleation theory's (CNT's) treatment of daughter-phase nucleation in a metastable parent phase. CNT asserts that the nucleation rate is directly proportional to the probability of any nucleation site gaining sufficient energy from its surroundings via thermal fluctuations to surmount the barrier preventing the new phase (or, in this case, stable dislocation loop) from forming; this is the origin of the Boltzmann-factor dependence in Eq. (16). The shear-stress-dependent factor in square brackets expresses the leading-order reduction of the nucleation barrier owed to the work done in prestressing the crystal. Classical MD simulations have shown that, when initially defect-free crystals are subjected to shear strains beyond their limit of mechanical stability, the rate at which dislocations homogeneously nucleate does indeed vary with shear stress and temperature in a manner consistent with the Arrhenius-like form in Eq. (16) [43].

TABLE I. Crystal plasticity model parameters.

Param.	Value	Units	Param.	Value	Units
$C_{0,11}$	274.8[a]	GPa	m_{11}	-0.0245	GPa K^{-1}
$C_{0,12}$	165.6[a]	GPa	m_{12}	-0.0118	GPa K^{-1}
$C_{0,44}$	87.2[a]	GPa	m_{44}	-0.0149	GPa K^{-1}
χ_{11}	4.22[a]		χ_{12}	2.78[a]	
χ_{44}	0.71[a]				
v_0	250[d]	ms^{-1}	τ_0	1.05[d]	GPa
ΔG_0	0.9×10^{-19}[d]	J	p	0.5[d]	
q	1.5[d]		$\tau_{0,\text{D}}$	1.6[d]	GPa
τ_{off}	2.3[d]	GPa	v_s	2000[d]	ms^{-1}
v_{off}	870[d]	ms^{-1}	R	10^{17}[b]	m^{-2}
b	2.86×10^{-10}[a]	m	$\rho_{\text{sat,min}}$	5×10^{10}	m^{-2}
$\rho_{\text{sat,0}}$	5×10^{19}[c]	m^{-2}	$\dot{\gamma}_{\text{sat}}$	10^{10}[c]	s^{-1}
N_{sat}	1.3[c]		λ	0.1	
$\dot{\rho}_0$	1.1×10^{28}[e]	$\text{m}^{-2}\text{s}^{-1}$	g_{nuc}	0.14[f]	
$\tau_{\text{nuc},0}$	5.5[f]	GPa			

[a] Derived from DFT simulations in Ref. [38].
[b] From Ref. [7].
[c] Fitted to multiscale modeling data from Ref. [7].
[d] Fitted to MD simulations using the SNAP tantalum potential.
[e] From Ref. [42].
[f] Fitted to Wehrenberg *et al.* [11] lattice rotation data.

While Eq. (16) was originally formulated to model the nucleation of (perfect) dislocations, we use it here as a proxy for nucleation processes in general, including deformation twinning. In tantalum, twinning effects plastic deformation along the same directions $\{\mathbf{m}_0^{\alpha}\} = \langle 111 \rangle$ and planes $\{\mathbf{n}_0^{\alpha}\} = \{211\}$ as full slip. The two processes are therefore kinematically equivalent [see Eq. (5)] and cause rotation of the host lattice about the same axes. Twinning may therefore be modeled as a pseudoslip mechanism that contributes additively to the deformation rates on the original slip systems α, an approach originally proposed in Ref. [44] and now widely used.

Parameters $\tau_{\text{nuc},0}$ and g_{nuc} were evaluated by fitting the locus of final lattice rotation states versus shock pressure to the experimental data. The value of $\tau_{\text{nuc},0}$ required to reproduce the sharp onset of deformation twinning above ∼25 GPa observed by Wehrenberg *et al.* [11,45] was approximately 5.5 GPa. This figure is consistent with the typical nucleation thresholds predicted by classical MD simulations of tantalum loaded along [001] [17]; we will compare these values in more detail and discuss sources of uncertainty in $\tau_{\text{nuc},0}$ in Sec. V.

To make more apparent the critical role of homogeneous nucleation, we will hereafter differentiate between two versions of our model: Model 1 will refer to the model without a nucleation term [i.e., retaining only the first two terms of Eq. (13)] and Model 2 will refer to the full model. A complete list of the model parameters' values and origins is given in Table I.

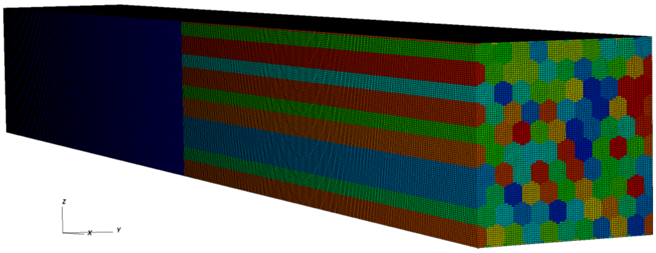

FIG. 1. Meshes and grain morphology used for all crystal plasticity finite element simulations of [110] fiber-textured tantalum polycrystals under dynamic compression. Cells in the target proper (right) are colored according to crystallographic orientation; cells in the flyer plate (left) are colored blue.

III. METHODOLOGY

A. Simulation setup

Figure 1 pictures our simulation geometry, which consists of a "flyer plate" and a sample, each of dimensions $4 \times 1 \times 1\ \mu\text{m}^3$. Zero-velocity boundary conditions on the y (z) component of velocity at the y (z) simulation cell boundaries are applied to simulate the average effect of inertial confinement due to the extended experimental sample in those transverse directions. Errors due to this boundary condition are minimal and are further mitigated by our calculating integrated quantities from a central, core region of the sample, excluding material less than $0.1\ \mu\text{m}$ from the y and z boundaries. These edge effects can be further mitigated by the use of periodic boundary conditions, which were unavailable to us here.

A shock wave is generated in the sample material by imparting an initial velocity in the $+x$ direction to the flyer plate, so that it impacts the front surface of the sample. The flyer-plate and sample regions are "meshed up" with cubic finite elements of side length 10 nm. The sample consists of columnar grains aligned with the loading axis x, with hexagonal cross sections of diameter $0.1\ \mu\text{m}$, which is broadly consistent with the grain sizes and morphology of the deposited samples used in the experiment of Wehrenberg *et al.* [11]. Grain orientations are sampled randomly from an orientation distribution function (ODF) representing a [110] fiber texture aligned with the x axis, with a spread in the angle between the [110] axis and the x axis given by a Gaussian with full width at half maximum (FWHM) of 4°.

While the experimental data of Wehrenberg *et al.* extend up to shock pressures of 260 GPa, our study is limited to pressures below 136 GPa; beyond this threshold, numerical difficulties are encountered by the FEM framework's iterative solver. While unfeasible here due to limits on available computational resources, this problem could be mitigated by reducing the simulation time step.

B. Diffraction calculation

Femtosecond x-ray diffraction was the primary diagnostic exploited by Wehrenberg *et al.* to characterize tantalum under extreme loading conditions. To facilitate comparisons between their experiment and our model, we generated synthetic diffraction patterns from our simulated samples. The CPFE code tracks the elastic deformation gradient field $\mathbf{F}_e(\mathbf{x})$ expressing the local orientation and distortion of the sample's crystal structure. At each material point, the deformed scattering plane normals $\hat{\mathbf{n}}_i$ may be calculated from the original planes $\hat{\mathbf{n}}_{i,0}$ using Eq. (3), effectively describing the transformation of the sample's reciprocal lattice vectors $\mathbf{G}_i$. Using the method described by MacDonald *et al.* [20], we can solve the Laue equation $\mathbf{k} - \mathbf{k}_0 = \mathbf{G}$ (where $\mathbf{k}_0$ and $\mathbf{k}$ are the incident and scattered x-ray wave vectors, respectively) and thus predict the diffraction pattern generated by our simulated samples under the x-ray geometry used by Wehrenberg *et al.* By simulating diffraction from full-field CPFE in this way, we are able to overcome the limitations suffered by earlier works simulating diffraction from dynamically compressed specimens, which have often used the assumptions of isotropic yield strength and/or polycrystalline homogenization assumptions based on the classic Voigt or Reuss models [19,20]. Calculation of diffraction patterns using high-fidelity models like MD or CPFE (see, for example, Refs. [21–25]) allows us to link XRD to complex processes of texture evolution and grain-grain interactions.

To calculate the scattering intensity generated by each reciprocal lattice vector, we first calculate its deviation from the ideal Bragg condition,

$$\Delta\theta_{\mathrm{B}} = \arcsin\left(\frac{|\mathbf{G}|}{2|\mathbf{k}_0|}\right) + \arcsin\left(\frac{\mathbf{k}_0 \cdot \mathbf{G}}{|\mathbf{k}_0||\mathbf{G}|}\right), \qquad (17)$$

following Ref. [20]. The relative scattering intensity can then be calculated by sampling a material rocking curve at the calculated value of $\Delta\theta_{\mathrm{B}}$. In this work, we assume that the rocking curve is a top-hat function centered around the ideal Bragg angle, such that if $|\Delta\theta_{\mathrm{B}}| < 0.2^\circ$ then scattering occurs with unit intensity; otherwise scattering does not occur.

Once all reciprocal lattice vectors have been summed over, the diffraction patterns are visualized by binning the scattering events from all finite elements into the $\phi - 2\theta_B$ plane, where ϕ is the azimuthal angle measured around the Debye-Scherrer ring.

C. Rotation calculation

The key point of comparison between our model and the experiment is the total amount of plasticity-induced lattice rotation as a function of shock pressure. Reorientation of the crystal structure was measured *in situ* by Wehrenberg *et al.* using the change in azimuthal positions of certain diffraction peaks. The same average reorientation can be calculated directly from our simulations using an appropriate decomposition and binning of the elastic deformation gradient field $\mathbf{F}_e(\mathbf{x})$. However, the experimental geometry of Wehrenberg *et al.* is such that only certain components of $\mathbf{F}_e$ can be measured. In this section, we clarify which components are measurable and what is meant by "the rotation."

In general, the crystal structure of a dynamically compressed metallic specimen that deforms plastically will both rotate and suffer pure shear strain [13], due to the stringent boundary conditions placed on the specimen by its inertial confinement in the transverse directions. Both pure rotation and pure shear alter the directions of atomic planes (which is ultimately what one measures with x-ray diffraction), meaning care must be taken when describing changes to the sample's crystal structure. For the present tantalum specimens, the plastically deformed material behind the shock front exhibits minimal deviatoric elastic strains, meaning the rotation component of $\mathbf{F}_e$ is primarily responsible for changing the directions of atomic planes. The postshock orientation of the planes [Eq. (3)] can therefore be approximated well as

$$\hat{\mathbf{n}} = \hat{\mathbf{n}}_0(\mathbf{Q}_e)^T. \tag{18}$$

That is, any and all changes to the directions of the crystal's atomic planes can be ascribed to pure rotation.

Wehrenberg *et al.* expressed the changes in crystallite orientation via the angle χ, defined as that between the sample normal and the normal to a given lattice plane producing a diffraction spot. For the ring of {110} peaks, the ambient spot initially situated at $\chi = 90^\circ$ remains centered on the $\chi = 90^\circ$ contour on compression, which is to say that the planes producing this diffraction do not change orientation. This is because the majority of the rotation suffered by the crystal takes place within this (local) plane. By contrast, the $\chi = 60^\circ$ diffraction peaks split into two upon compression, since the corresponding diffracting plane rotates away from the compression axis.

The degree of grain rotation is derived by assuming that *all* of the rotation occurs within the $\chi = 90^\circ$ plane and applying an appropriate geometrical transformation to recover the full rotation magnitude. Due to the azimuthal symmetry of the fiber-textured samples, the experiment is insensitive to any rotation that might occur around the axis defined by the sample normal.

For consistency with the experiment, we chose a measure of rotation that excludes rotation around the sample normal vector: most of the rotation occurs in the {110} plane making an angle $\chi \approx 90^\circ$ with the sample normal. This plane contains both the sample normal and normals of the two predominant slip planes (which are mirror images of one another). We identify the specific $\langle 002\rangle$ vector that lies in this plane of rotation and then calculate χ for this vector both before and after deformation. We then calculate

$$Q = \Delta\chi = \chi_{\text{deformed}} - \chi_{\text{ambient}} \tag{19}$$

for this $\langle 002\rangle$ vector. The resulting distribution of rotation angles is then either arithmetically averaged or fitted to a peak function over the appropriate set of finite elements to derive values for the "macroscopic rotation"—which of these two rotation metrics is used at each point Sec. IV will be made clear at the relevant juncture.

IV. RESULTS

We performed dynamic compression simulations of fiber-textured tantalum polycrystals up to shock pressures of 136 GPa and analyzed their plastic response, characterizing the combination of plasticity mechanisms that became active, the density and dynamics of the dislocations mediating the plastic flow, and the concomitant lattice rotation. Figure 2(a) provides an overview of the dynamic response of samples simulated under Model 2 at pressures of 16, 35, and 79 GPa. As anticipated, we observe steep compression waves that elevate the longitudinal elastic strain $\varepsilon_{e,L}$ to between ~5% and 15%, followed by rapid creation and motion of dislocations that mediate plastic deformation and relieve the majority of the deviatoric stresses and elastic strains. This relaxation is accompanied by substantial lattice rotation Q whose magnitude increases monotonically—though in a nontrivial way—with shock pressure. Our simulations allow us to examine in detail the spatial distribution of this rotation and to explain its interesting dependence on pressure by analyzing the activity of the plasticity mechanisms activated by the compression wave.

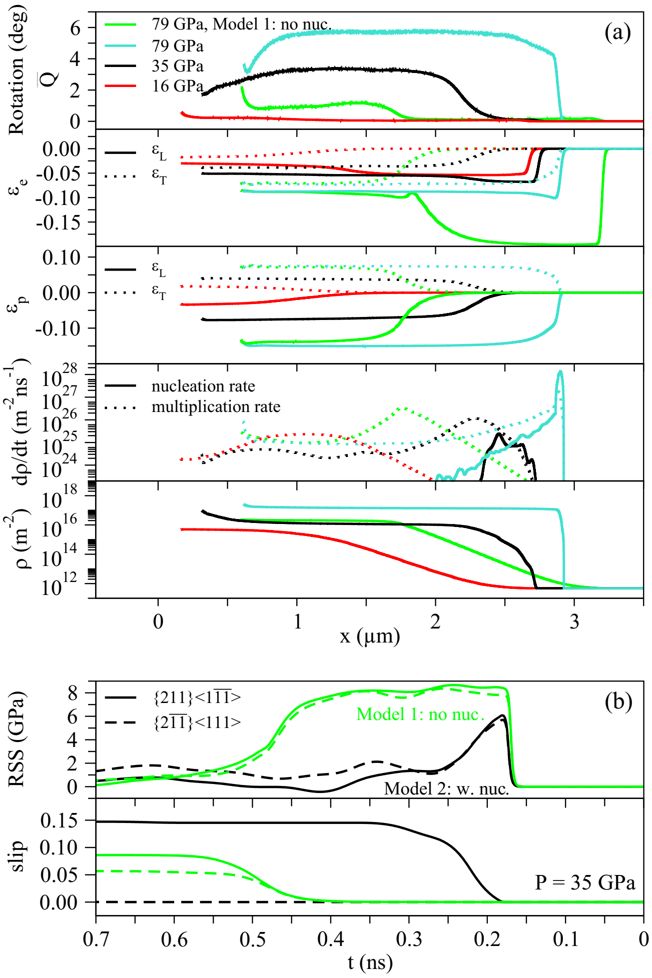

FIG. 2. (a) Profiles of various quantities along the loading direction (x) at time $t = 0.6$ ns, averaged over the lateral directions y and z, taken from simulations using Model 2 unless otherwise stated. The average lattice rotation $\bar{Q}$, the elastic and plastic strains ε_e and ε_p, dislocation growth rates $d\rho/dt$, and the dislocation density ρ are shown. (b) Time series of the resolved shear stress (RSS) τ^α and slip-system activity γ^α for the two dominant slip systems, from the $P = 35$ GPa simulations, from a material point located at (1.00, 0.83, 0.52) μm.

In Fig. 3, we show how the rotation varies across the cross section of the sample at a shock pressure of 35 GPa. The spatial distribution of the rotation (as expressed in the simulation cell basis) correlates strongly with the underlying grain morphology. Part of this spatial variation can be explained by the fact that, within each grain, lattice rotation takes place predominantly about a preferred *crystallographic* direction, meaning the rotation matrix $\mathbf{Q}_e$ is nonuniform in the "laboratory" frame. However, even after accounting for this,

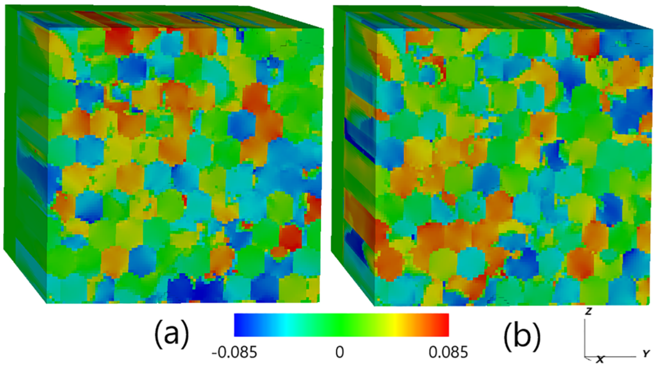

FIG. 3. Rotation matrix elements (a) Q_{12} and (b) Q_{13}, for the 35 GPa shock at $t = 0.6$ ns, and a slice at $x = 1$ μm, significantly behind the shock front, using Model 2. These matrix elements represent reasonable approximations to the lattice rotation (in radians) about the z and y axes, respectively. Morphology of domains of similar rotation correlate with the grain scale, though significant heterogeneity occurs within grains too.

there is still significant intragranular heterogeneity and some grains exhibit regions that rotate in opposite directions. Figure 4 shows the distribution of local rotation angles as defined by Eq. (19) (which measures the reorientation around each grain's dominant rotation axis) at pressures of 16, 35, 79, and 136 GPa. The degree of lattice rotation behind the shock front is distributed with an approximately Gaussian spread around a nonzero central value that increases with pressure. Note that the rotation distribution at the lowest shock pressure of 16 GPa has a remarkably small modal value, smaller even than one would expect from extrapolating the higher-pressure data (which would yield $\Delta\chi \sim 2^\circ$); this is an important point we will return to shortly. The key observation is that despite considerable heterogeneity, the average degree of lattice rotation grows with shock pressure, as observed by Wehrenberg *et al.*

To confirm that the CPFE simulations predict the correct dominant rotation axis, we compare in Fig. 5 a representative diffractogram obtained by Wehrenberg *et al.* with a synthetic diffraction pattern calculated from a simulation at a comparable shock pressure using the method described in Sec. III B. We see strong agreement between the measured and modeled diffraction patterns. Crucially, the CPFE simulations predict that scattering peaks along the $\chi = 60^\circ$ contour split in two upon compression, while those along $\chi = 90^\circ$ do not. The sense of the rotation is therefore correctly predicted by our model.

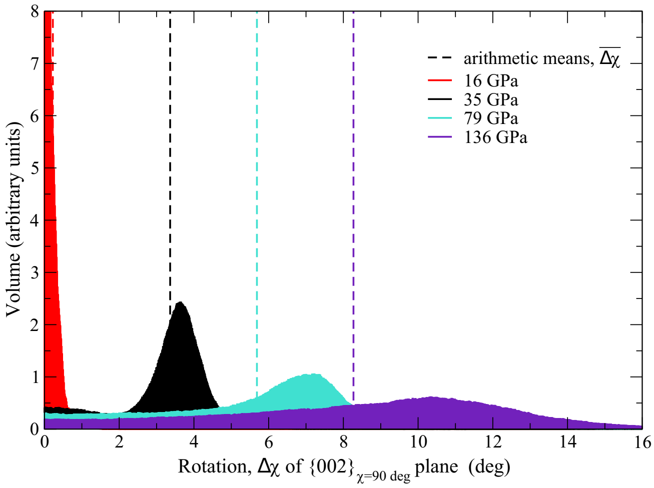

FIG. 4. Histograms showing the shock-pressure-dependent distribution of lattice rotations behind the shock front for tantalum polycrystals modeled with Model 2.

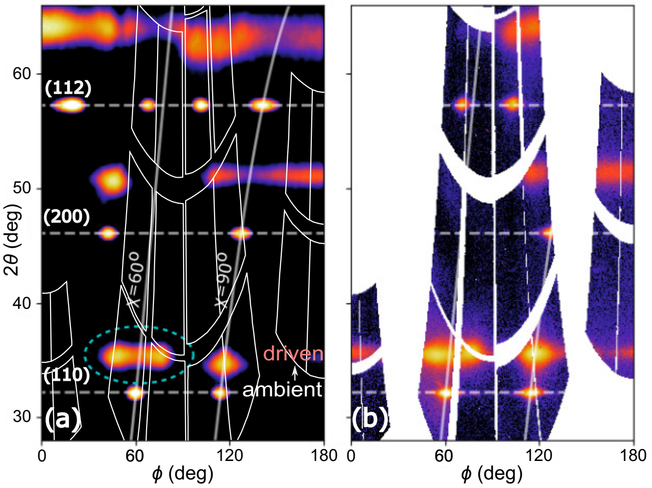

FIG. 5. Diffraction patterns (a) calculated from simulation of a 105 GPa shock and (b) taken from an experimental shot at 109 GPa. The x-ray probe energy is 9.6 keV. Simulated pattern is taken from a snapshot at time $t = 0.6$ ns, when the shock front has traveled approximately three quarters of the way through the sample. Both ambient and driven spots are visible. Splitting of the $\chi = 60^\circ$ texture spot (see within the cyan colored dashed ring) indicates lattice rotation.

We also compare in Fig. 6 the magnitude of plasticity-induced rotation predicted by our model (blue line) with that

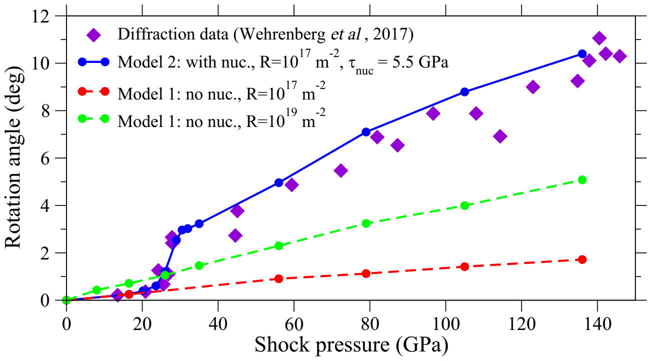

FIG. 6. Plasticity-induced lattice rotation in shock-loaded tantalum from the x-ray diffraction experiment of Wehrenberg *et al.* [11] and from CPFE modeling. Model 1, which is based on the LMS model [7] and accounts for dislocation multiplication and annihilation via the parameter R, fails to describe the locus of rotation states at pressures exceeding 27 GPa. Model 2, which additionally incorporates dislocation nucleation processes with a shear-stress threshold of $\tau_{\text{nuc},0} = 5.5$ GPa, captures both the low- and high-pressure regimes successfully.

extracted directly from Wehrenberg *et al.*'s diffraction data (purple points). The data allow us to identify two rotation regimes: one above a transition pressure of 27 GPa, where rotations are relatively large, and one below 27 GPa, where rotations are far smaller—smaller even than would be expected from the trend in the higher-pressure data. With the choice of model parameters given in Table I, Model 2 is able to reproduce the locus of rotation states relatively well across both rotation regimes. By contrast, Model 1—in which dislocation nucleation processes are "switched off"—matches the experimental data only below the critical threshold pressure of 27 GPa (red dashed line); in the high-pressure regime, the predicted rotation is far too low. We therefore conclude that the high-pressure lattice rotation observed by Wehrenberg *et al.* cannot be explained without (and thus provide direct evidence for) dislocation nucleation. We will now elucidate how the nature of the plasticity and attendant lattice rotation change as one crosses the threshold between the two rotation regimes.

Figure 2(a) showed the dislocation multiplication and nucleation rates at pressures above and below the 27 GPa threshold. We see that at 16 GPa (i.e., below threshold) the only process that can increase the dislocation density ρ_{tot} is conventional multiplication, because the nucleation rate $\dot{\rho}^{\alpha}_{\text{nuc}}$ is vanishing on all slip systems. At 35 GPa (above threshold), nucleation becomes active at a level competitive with—or even exceeding—ordinary multiplication. This is consistent with the fact that in the low-pressure regime the RSS acting on the dominant slip systems never exceeds the threshold stress for nucleation of $\tau_{\text{nuc},0} = 5.5$ GPa, so that dislocation nucleation processes are effectively absent. The transition between the two rotation regimes at 27 GPa thus coincides with the activation of nucleation processes. This appears to be consistent with the experimental observation that the jump in rotation is also marked by the sudden onset of deformation twinning, for which our model's nucleation term in Eq. (16) acts as a proxy. It is clear, then, that transition is causally linked to the onset of nucleation. This begs the following question: why should dislocations nucleated homogeneously bring about greater lattice rotation than those created by multiplication?

The answer is *not* because dislocation nucleation permits a greater amount of plastic deformation overall. The single-slip model proposed in Wehrenberg *et al.* [11] related the degree of lattice rotation to the amount of plastic strain (though, as noted above, that simple model is not strictly valid under uniaxial conditions [13]) and predicted that the rotation increases monotonically with strain. However, the differences in the degree of rotation observed between Models 1 and 2 are too great to be explained by differing amounts of plastic strain. Figure 2(a) compares the response of the sample at 79 GPa under both Model 1 and Model 2 and shows that, while the final dislocation densities differ by an order of magnitude, the predicted total plastic deformation states far behind the shock front are nearly identical (though the relaxation time is longer for Model 1). Therefore, the large rotations brought about by a nucleation-dominated plastic flow process cannot be explained by differences in the total plastic strain; instead, we must examine how the plasticity is partitioned between the various slip systems.

In Fig. 2(b), we show the RSS on and activity of the two dominant slip systems at a representative material point located near the center of a grain cross section at position (1.00, 0.83, 0.52) μm, using both Models 1 and 2. As noted above, the *total* amount of slip predicted by the two models at a given shock pressure are comparable. However, Model 1 shares this slip relatively evenly between the two dominant slip systems ($\{211\}\langle 1\bar{1}\bar{1}\rangle$ and $\{2\bar{1}\bar{1}\}\langle 111\rangle$), whereas Model 2 distributes almost all of this slip to only one of the two slip systems. As discussed extensively by Heighway and Wark [46], the degree of rotation is related primarily to the difference in activity on the two competing slip systems, because slip on those systems generates rotation in mutually opposing directions. While there is some variation in the exact distribution of slip between the two slip systems at different points in the sample, it is the case everywhere that the majority of plasticity is apportioned to only one of these two dominant plasticity mechanisms.

The cause of the stark difference in slip-system activities in the regime dominated by dislocation nucleation is the amplified sensitivity of the rate of plastic deformation to the shear stresses driving it. During the elastic phase of the loading, there is a very small "seed" difference in the RSS acting on the two systems, resulting from two main sources: (1) elastic interactions at boundaries between neighboring grains [36] and (2) perturbations in the initial orientations of the grains away from perfect [110] alignment. In nucleation-aware Model 2, the plastic relaxation rate near the nucleation threshold is a very rapidly varying function of the RSS. Once the nucleation threshold is reached on the local slip system that experiences the slightly higher RSS, it mediates plastic deformation extremely quickly, which relieves the shear stress on *both* slip systems, so that the second slip system never reaches the nucleation threshold. With Model 1, the plastic relaxation rate at the shock front is a much more slowly varying function of the RSS, leading to a more equitable distribution of defect generation and slip between the two systems, better reflecting their initially similar RSSs and leading to a considerably reduced net rotation. A similar rotation-suppression effect from slip-slip competition has been observed in classical MD simulations of fcc copper shocked along [111] [46].

To confirm that it is dislocation nucleation—and only nucleation—that can explain the large rotations seen in experiment, we also calculated the rotation locus assuming a greatly enhanced dislocation multiplication rate; in principle, one could imagine that the contrast in slip-system activities (and therefore the net rotation) could be inflated by scaling up R and thus "magnifying" the initial seed discrepancy between the dominant slip systems. In Fig. 6, we show the pressure-dependent rotation that Model 1 predicts with a dislocation multiplication rate 100 times greater than the "true" fitted value (dashed green line). Even this greatly augmented multiplication rate (which in any case cannot be justified given that R is constrained by multiscale modeling [7]) cannot raise the rotation to the level observed in the data. Hence only the nucleation-aware version of our crystal plasticity model can satisfactorily explain the results of Wehrenberg *et al.*

V. DISCUSSION

The high-strain-rate crystal plasticity model we have put forward successfully predicts the slip-induced rotation observed in tantalum dynamically compressed to around a megabar. Critical to its success is its inclusion of the dislocation nucleation terms $\dot{\rho}^{\alpha}_{\mathrm{nuc}}$, which can account for the sudden increase in net rotation above shock pressures of 27 GPa. This transition pressure is determined by the balance between the rates of the competing multiplication and nucleation processes. Here, we have assumed that the parametrization of the multiplication process used in the LMS model is accurate (with $R = 10^{17}\ \mathrm{m}^{-2}$). This value of R necessitates a characteristic nucleation threshold stress $\tau_{\mathrm{nuc},0}$ of 5.5 GPa for agreement between the model and the data. Here, we discuss whether this is a realistic nucleation threshold and how tightly its value is constrained by the data.

The nucleation of plasticity agents in tantalum was explored via large-scale, classical MD simulations by Zepeda-Ruiz *et al.* [17]. While uniaxially stressing tantalum monocrystals along [001] at high strain rates, they found that the RSS required to heterogeneously nucleate deformation twins from existing defects was (1.9 ± 0.3) GPa. When deprived of hetereogeneous nucleation sources, the RSS for twin nucleation increased to approximately 8.4 GPa. We would expect the characteristic nucleation stress $\tau_{\mathrm{nuc},0}$ parametrizing the total nucleation rate $\dot{\rho}^{\alpha}_{\mathrm{nuc}}$ to be an appropriately weighted average of the activation stresses of the various processes for which it is acting as a proxy. In this respect, we believe an activation shear stress of 5.5 GPa that sits between the heterogeneous (lower) and homogeneous (upper) limits of 1.9 and 8.4 GPa to be physically reasonable. We note that the values of these limits should not be taken at face value, obtained as they are from MD simulations using traditional, classical interatomic potentials that are bound to be inaccurate to some degree. Moreover, non-Schmid effects typical of slip in bcc crystals [47] mean that the critical RSS for deformation twinning may depend upon the direction of the loading, hampering a direct comparison between the [001] tantalum simulated by Zepeda-Ruiz *et al.* and the [110] tantalum studied here. Even so, we maintain that $\tau_{\mathrm{nuc},0} = 5.5$ GPa lies in the expected region for a nucleation threshold.

It is also important to consider the value of the dislocation nucleation *activation volume* implied by our model. The dislocation nucleation rate $\dot{\rho}^{\alpha}_{\mathrm{nuc}}$ in Eq. (16) may be recast into the generic form

$$\dot{\rho}^{\alpha}_{\mathrm{nuc}} = \dot{\rho}_0 \exp\left(-\frac{\varepsilon - \tau^{\alpha}_{\mathrm{eff}} v^*}{k_B T}\right), \tag{20}$$

where ε is the ambient enthalpy barrier against nucleation and the activation volume v^* is essentially the volume of material involved in the nucleation process. In our parametrization scheme, $v^* \equiv g_{\mathrm{nuc}}(C_{0,44}/\tau_{\mathrm{nuc},0})b^3 \sim 2.2b^3$, equivalent to $2.9\Omega_0$ (Ω_0 being the ambient atomic volume). This is of the expected order of magnitude for a dislocation nucleation event, involving as it does the reconfiguration of a few unit cells. To make a quantitative comparison with literature values of v^* is challenging due to the disparate natures of dynamic compression, which we consider here, and nanoindentation, whence the vast majority of existing measurements are derived; it is not immediately clear in either scenario whether it is homogeneous or heterogeneous nucleation that is primarily being probed, making a like-for-like comparison difficult.

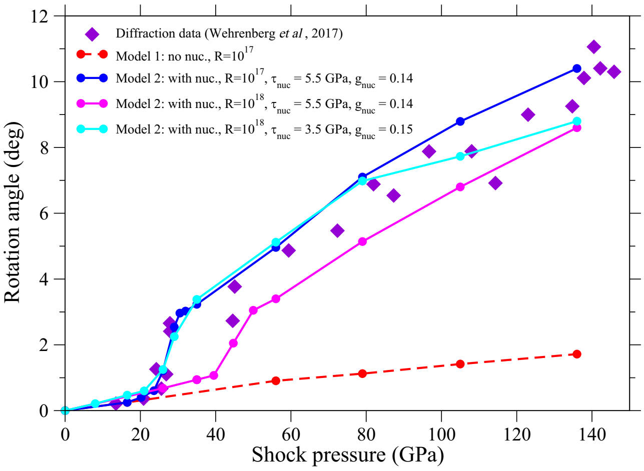

FIG. 7. Plasticity-induced lattice rotation in shock-loaded tantalum from the x-ray diffraction experiment of Wehrenberg *et al.* [11] and predicted by different iterations of CPFE Model 2. The predicted transition shock pressure is determined by the balance between the multiplication and nucleation rates, which are parametrized by variables R and $\tau_{\mathrm{nuc},0}$, respectively.

With this in mind, we note that nanoindentation studies put the nucleation activation volume of single-crystal tantalum in the region 0.2–$0.9b^3$ [48] and that of nanopillared molybdenum (another bcc metal in the same family of refractory metals as tantalum) between 0.8 and $1.4b^3$ [49]. Our fitted value of $2.2b^3$ therefore sits at the higher end of the range of values anticipated from nanoindentation studies, which may indicate that homogeneous nucleation (which involves relatively large critical nuclei) is more prevalent a nucleation mode than heterogeneous nucleation in this shock-loading scenario [50]. In any case, we regard the activation volume required of the model to be a physically reasonable value.

While the model parameters $\tau_{\mathrm{nuc},0}$ and g_{nuc} that we have introduced to describe defect nucleation are fitted directly from experimental data, the remainder (see Table I) are derived from various simulations conducted over a range of length scales. A degree of uncertainty in $\tau_{\mathrm{nuc},0}$ and g_{nuc} therefore arises from uncertainties in the remaining parameters; from a fitting perspective, all parameters covary to some extent and it transpires that, when fitting to the present data, $\tau_{\mathrm{nuc},0}$ is particularly sensitive to changes in R, the dislocation multiplication rate. This is because the transition shock pressure in our model is determined by the balance between the rates of multiplication and nucleation. In Fig. 7, we show the effect of increasing the multiplication rate in Model 2 by a factor of 10 (to $R = 10^{18}\ \mathrm{m}^{-2}$). The ability of the enhanced multiplication rate to keep the RSSs below the nucleation threshold elevates the transition pressure from 27 to 45 GPa (pink curve). To push this transition pressure back down to the value observed experimentally, the nucleation threshold must be reduced to $\tau_{\mathrm{nuc},0} = 3.5$ GPa (while v^* becomes $3.7b^3$); this new combination of parameters recreates the data just as well as the fitted values quoted in Table I. We note that it has been suggested that heterogeneous dislocation nucleation could be activated in the weak-shock regime in fcc aluminium [51] and bcc tantalum [52] (processes not accounted for in the present modeling), making it conceivable that the multiplication rate R could be higher than that suggested by the LMS. This would necessitate a lower value of $\tau_{\mathrm{nuc},0}$.

It would therefore be profitable, in further work, to fully characterize the covariance of the fitting parameters in our crystal plasticity model and hence to provide a definitive bound on the range of values they can obtain. It would also be informative to perform MD simulations of dislocation nucleation under extreme stresses to confirm that the value of the model parameter g_{nuc} (which expresses the activation volume) obtained from the data is realistic; the activation volume can be evaluated by measuring the temperature and shear-stress dependence of the dislocation nucleation rate, as done in the computational study of Norman and Yanilkin [43].

VI. CONCLUSION

We have constructed a crystal plasticity model that provides a description unifying the phenomenology of the dynamic compression experiment of Wehrenberg *et al.* [11] in both the small- and large-rotation regimes. We have thus overcome the limitations of previous modeling, including MD simulations, which was limited in its capacity to address regimes of realistic polycrystalline microstructures and nonoverdriven shocks. We have generated synthetic diffraction patterns from our modeling, going beyond previous mean-field approaches, permitting the link between XRD and complex texture evolution to be analyzed. We reproduced many of the salient features of the experimental patterns, including the splitting (or nonsplitting) of various texture spots. The lattice rotation data from the experiment is well represented by our model, which accounts for both dislocation multiplication from preexisting dislocations (based closely on the LMS model) and dislocation nucleation processes that activate when the resolved shear stress exceeds a critical threshold of 5.5 GPa. The inclusion of these latter processes proved crucial to the success of the model. We used the data of Wehrenberg *et al.* to constrain directly the rate equations for plastic deformation kinetics during a shock. The excellent agreement of the diffraction data with these CPFE simulations demonstrates how multiscale models can inform our understanding of detailed lattice-level plasticity at ultrahigh strain rates.

ACKNOWLEDGMENTS

P.G.H. and J.S.W. gratefully acknowledge support from AWE via the Oxford Centre for High Energy Density Science (OxCHEDS). J.S.W. is also grateful for support from EPSRC under Grant No. EP/S025065/1. This work was performed under the auspices of the US Department of Energy by Lawrence Livermore National Laboratory under Contract No. DE-AC52-07NA27344. UK Ministry of Defence © Crown Owned Copyright 2023/AWE.

[1] E. Asphaug, C. B. Agnor, and Q. Williams, Hit-and-run planetary collisions, Nature (London) **439**, 155 (2006).

[2] R. M. Canup and E. Asphaug, Origin of the moon in a giant impact near the end of the earth's formation, Nature (London) **412**, 708 (2001).

[3] L. E. Senft and S. T. Stewart, Modeling impact cratering in layered surfaces, J. Geophys. Res. **112**, E11002 (2007).

[4] R. E. Rudd, T. C. Germann, B. A. Remington, and J. S. Wark, Metal deformation and phase transitions at extremely high strain rates, MRS Bull. **35**, 999 (2010).

[5] H.-S. Park, R. E. Rudd, R. M. Cavallo, N. R. Barton, A. Arsenlis, J. L. Belof, K. J. M. Blobaum, B. S. El-dasher, J. N. Florando, C. M. Huntington, B. R. Maddox, M. J. May, C. Plechaty, S. T. Prisbrey, B. A. Remington, R. J. Wallace, C. E. Wehrenberg, M. J. Wilson, A. J. Comley, E. Giraldez *et al.*, Grain-size-independent plastic flow at ultrahigh pressures and strain rates, Phys. Rev. Lett. **114**, 065502 (2015).

[6] B. A. Remington, H.-S. Park, D. T. Casey, R. M. Cavallo, D. S. Clark, C. M. Huntington, C. C. Kuranz, A. R. Miles, S. R. Nagel, K. S. Raman, and V. A. Smalyuk, Rayleigh–Taylor instabilities in high-energy density settings on the national ignition facility, Proc. Natl. Acad. Sci. USA **116**, 18233 (2019).

[7] N. R. Barton, J. V. Bernier, R. Becker, A. Arsenlis, R. Cavallo, J. Marian, M. Rhee, H.-S. Park, B. A. Remington, and R. T. Olson, A multiscale strength model for extreme loading conditions, J. Appl. Phys. **109**, 073501 (2011).

[8] C. E. Wehrenberg, A. J. Comley, N. R. Barton, F. Coppari, D. Fratanduono, C. M. Huntington, B. R. Maddox, H.-S. Park, C. Plechaty, S. T. Prisbrey, B. A. Remington, and R. E. Rudd, Lattice-level observation of the elastic-to-plastic relaxation process with subnanosecond resolution in shock-compressed Ta using time-resolved *in situ* Laue diffraction, Phys. Rev. B **92**, 104305 (2015).

[9] M. J. Suggit, A. Higginbotham, J. A. Hawreliak, G. Mogni, G. Kimminau, P. Dunne, A. J. Comley, N. Park, B. A. Remington, and J. S. Wark, Nanosecond white-light Laue diffraction measurements of dislocation microstructure in shock-compressed single-crystal copper, Nat. Commun. **3**, 1224 (2012).

[10] D. Milathianaki, S. Boutet, G. J. Williams, A. Higginbotham, D. Ratner, A. E. Gleason, M. Messerschmidt, M. M. Seibert, D. C. Swift, P. Hering, J. Robinson, W. E. White, and J. S. Wark, Femtosecond visualization of lattice dynamics in shock-compressed matter, Science **342**, 220 (2013).

[11] C. E. Wehrenberg, D. McGonegle, C. Bolme, A. Higginbotham, A. Lazicki, H. J. Lee, B. Nagler, H. S. Park, B. A. Remington, R. E. Rudd, M. Sliwa, M. Suggit, D. Swift, F. Tavella, L. Zepeda-Ruiz, and J. S. Wark, *In situ* x-ray diffraction measurement of shock-wave-driven twinning and lattice dynamics, Nature (London) **550**, 496 (2017).

[12] E. Schmid, Über die schubverfestigung von einkristallen bei plastischer deformation, Z. Phys. **40**, 54 (1926).

[13] P. G. Heighway and J. S. Wark, Kinematics of slip-induced rotation for uniaxial shock or ramp compression, J. Appl. Phys. **129**, 085109 (2021).

[14] R. Ravelo, T. C. Germann, O. Guerrero, Q. An, and B. L. Holian, Shock-induced plasticity in tantalum single crystals: Interatomic potentials and large-scale molecular-dynamics simulations, Phys. Rev. B **88**, 134101 (2013).

[15] A. Higginbotham, M. J. Suggit, E. M. Bringa, P. Erhart, J. A. Hawreliak, G. Mogni, N. Park, B. A. Remington, and J. S.

Wark, Molecular dynamics simulations of shock-induced deformation twinning of a body-centered-cubic metal, Phys. Rev. B **88**, 104105 (2013).

[16] D. Tramontina, P. Erhart, T. Germann, J. Hawreliak, A. Higginbotham, N. Park, R. Ravelo, A. Stukowski, M. Suggit, Y. Tang, J. Wark, and E. Bringa, Molecular dynamics simulations of shock-induced plasticity in tantalum, High Energy Density Phys. **10**, 9 (2014).

[17] L. A. Zepeda-Ruiz, A. Stukowski, T. Oppelstrup, and V. V. Bulatov, Probing the limits of metal plasticity with molecular dynamics simulations, Nature (London) **550**, 492 (2017).

[18] L. A. Zepeda-Ruiz, A. Stukowski, T. Oppelstrup, N. Bertin, N. R. Barton, R. Freitas, and V. V. Bulatov, Atomistic insights into metal hardening, Nat. Mater. **20**, 315 (2021).

[19] A. Higginbotham and D. McGonegle, Prediction of Debye-Scherrer diffraction patterns in arbitrarily strained samples, J. Appl. Phys. **115**, 174906 (2014).

[20] M. J. MacDonald, J. Vorberger, E. J. Gamboa, R. P. Drake, S. H. Glenzer, and L. B. Fletcher, Calculation of Debye-Scherrer diffraction patterns from highly stressed polycrystalline materials, J. Appl. Phys. **119**, 215902 (2016).

[21] G. Kimminau, B. Nagler, A. Higginbotham, W. J. Murphy, N. Park, J. Hawreliak, K. Kadau, T. C. Germann, E. M. Bringa, D. H. Kalantar, H. E. Lorenzana, B. A. Remington, and J. S. Wark, Simulating picosecond x-ray diffraction from shocked crystals using post-processing molecular dynamics calculations, J. Phys.: Condens. Matter **20**, 505203 (2008).

[22] A. Higginbotham, J. Hawreliak, E. M. Bringa, G. Kimminau, N. Park, E. Reed, B. A. Remington, and J. S. Wark, Molecular dynamics simulations of ramp-compressed copper, Phys. Rev. B **85**, 024112 (2012).

[23] M. J. Echeverria, S. Galitskiy, A. Mishra, R. Dingreville, and A. M. Dongare, Understanding the plasticity contributions during laser-shock loading and spall failure of Cu microstructures at the atomic scales, Comput. Mater. Sci. **198**, 110668 (2021).

[24] A. Mishra, C. Kunka, M. J. Echeverria, R. Dingreville, and A. M. Dongare, Fingerprinting shock-induced deformations via diffraction, Sci. Rep. **11**, 9872 (2021).

[25] D. Francom, D. J. Walters, J. L. Barber, D. J. Luscher, E. Lawrence, A. Biswas, C. M. Biwer, D. Banesh, J. Lazarz, S. C. Vogel, K. Ramos, C. Bolme, R. L. Sandberg, and J. Ahrens, Simulation and emulation of x-ray diffraction from dynamic compression experiments, J. Dynam. Behav. Mater. **7**, 170 (2021).

[26] T. Nguyen, S. J. Fensin, and D. J. Luscher, Dynamic crystal plasticity modeling of single crystal tantalum and validation using Taylor cylinder impact tests, Int. J. Plast. **139**, 102940 (2021).

[27] R. Becker, Effects of crystal plasticity on materials loaded at high pressures and strain rates, Int. J. Plast. **20**, 1983 (2004), Daniel C. Drucker Memorial Issue.

[28] C. Bronkhorst, B. Hansen, E. Cerreta, and J. Bingert, Modeling the microstructural evolution of metallic polycrystalline materials under localization conditions, J. Mech. Phys. Solids **55**, 2351 (2007).

[29] C. Bronkhorst, S. Kalidindi, and L. Anand, Polycrystalline plasticity and the evolution of crystallographic texture in fcc metals, Philos. Trans. R. Soc. A **341**, 443 (1992).

[30] S. Kalidindi, C. Bronkhorst, and L. Anand, Crystallographic texture evolution in bulk deformation processing of fcc metals, J. Mech. Phys. Solids **40**, 537 (1992).

[31] G. Whiteman, S. Case, J. Millett, M. Cox, P. Avraam, J. Dear, A. Sancho, and P. Hooper, Uniaxial compression of single crystal and polycrystalline tantalum, Mater. Sci. Eng., A **759**, 70 (2019).

[32] C. R. Weinberger, B. L. Boyce, and C. C. Battaile, Slip planes in bcc transition metals, Int. Mater. Rev. **58**, 296 (2013).

[33] L. M. Hale, J. A. Zimmerman, and C. R. Weinberger, Simulations of bcc tantalum screw dislocations: Why classical inter-atomic potentials predict 112 slip, Comput. Mater. Sci. **90**, 106 (2014).

[34] C. Woodward and S. I. Rao, Flexible *ab initio* boundary conditions: Simulating isolated dislocations in bcc Mo and Ta, Phys. Rev. Lett. **88**, 216402 (2002).

[35] L. Smith, J. A. Zimmerman, L. M. Hale, and D. Farkas, Molecular dynamics study of deformation and fracture in a tantalum nano-crystalline thin film, Modell. Simul. Mater. Sci. Eng. **22**, 045010 (2014).

[36] P. G. Heighway, D. McGonegle, N. Park, A. Higginbotham, and J. S. Wark, Molecular dynamics simulations of grain interactions in shock-compressed highly textured columnar nanocrystals, Phys. Rev. Mater. **3**, 083602 (2019).

[37] H. Lim, J. D. Carroll, J. R. Michael, C. C. Battaile, S. R. Chen, and J. M. D. Lane, Investigating active slip planes in tantalum under compressive load: Crystal plasticity and slip trace analyses of single crystals, Acta Mater. **185**, 1 (2020).

[38] P. Söderlind and J. A. Moriarty, First-principles theory of Ta up to 10 Mbar pressure: Structural and mechanical properties, Phys. Rev. B **57**, 10340 (1998).

[39] G. Simmons and G. Wang, *Single Crystal Elastic Properties and Calculated Aggregate Properties: A Handbook* (MIT Press, Cambridge, MA, 1971).

[40] A. Thompson, L. Swiler, C. Trott, S. Foiles, and G. Tucker, Spectral neighbor analysis method for automated generation of quantum-accurate interatomic potentials, J. Comput. Phys. **285**, 316 (2015).

[41] R. E. Rudd, A. J. Comley, J. Hawreliak, B. Maddox, H.-S. Park, and B. A. Remington, Theory and simulation of 1D to 3D plastic relaxation in tantalum, AIP Conf. Proc. **1426**, 1379 (2012).

[42] R. A. Austin and D. L. McDowell, A dislocation-based constitutive model for viscoplastic deformation of fcc metals at very high strain rates, Int. J. Plast. **27**, 1 (2011).

[43] G. E. Norman and A. V. Yanilkin, Homogeneous nucleation of dislocations, Phys. Solid State **53**, 1614 (2011).

[44] P. Houtte, Simulation of the rolling and shear texture of brass by the Taylor theory adapted for mechanical twinning, Acta Metall. **26**, 591 (1978).

[45] M. Sliwa, D. McGonegle, C. Wehrenberg, C. A. Bolme, P. G. Heighway, A. Higginbotham, A. Lazicki, H. J. Lee, B. Nagler, H. S. Park, R. E. Rudd, M. J. Suggit, D. Swift, F. Tavella, L. Zepeda-Ruiz, B. A. Remington, and J. S. Wark, Femtosecond x-ray diffraction studies of the reversal of the microstructural effects of plastic deformation during shock release of tantalum, Phys. Rev. Lett. **120**, 265502 (2018).

[46] P. G. Heighway and J. S. Wark, Slip competition and rotation suppression in tantalum and copper during dynamic uniaxial compression, Phys. Rev. Mater. **6**, 043605 (2022).

[47] J. C. F. Millett, P. Avraam, G. Whiteman, D. J. Chapman, and S. Case, The role of orientation on the shock response of single crystal tantalum, J. Appl. Phys. **128**, 035104 (2020).

[48] O. Franke, J. Alcalá, R. Dalmau, Z. C. Duan, J. Biener, M. Biener, and A. Hodge, Incipient plasticity of single-crystal tantalum as a function of temperature and orientation, Philos. Mag. **95**, 1866 (2015).

[49] J.-Y. Kim, D. Jang, and J. R. Greer, Tensile and compressive behavior of tungsten, molybdenum, tantalum and niobium at the nanoscale, Acta Mater. **58**, 2355 (2010).

[50] J. K. Mason, A. C. Lund, and C. A. Schuh, Determining the activation energy and volume for the onset of plasticity during nanoindentation, Phys. Rev. B **73**, 054102 (2006).

[51] R. A. Austin, Elastic precursor wave decay in shock-compressed aluminum over a wide range of temperature, J. Appl. Phys. **123**, 035103 (2018).

[52] R. Kositski and D. Mordehai, On the origin of the stress spike decay in the elastic precursor in shocked metals, J. Appl. Phys. **126**, 085901 (2019).